VI International Conference on Computational Methods in Marine Engineering
MARINE 2015
F. Salvatore, R. Broglia and R. Muscari (Eds)

SOLUTION AND DOMAIN DECOMPOSITION MODEL FOR MARINE HYDRODYNAMICS: RANS AND POTENTIAL FLOW COUPLING

VUKO VUKČEVIĆ*, HRVOJE JASAK*,† AND ŠIME MALENICA‡

*University of Zagreb, Faculty of Mechanical Engineering and Naval Architecture
Ivana Lučića 5, Zagreb, Croatia
e-mail: vuko.vukcevic@fsb.hr, hrvoje.jasak@fsb.hr, web page: www.fsb.unizg.hr

† Wikki Ltd, 459 Southbank House, SE1 7SJ, London, United Kingdom
e-mail: h.jasak@wikki.co.uk, web page: wikki.co.uk

‡ Bureau Veritas, 67/71, 92200 boulevard du Château, Neuilly-sur-Seine, France
e-mail: sime.malenica@bureauveritas.com, www.bureauveritas.com

Key words: RANS and Potential Flow Coupling, Solution Decompositon, Wave Modelling, Free Surface

Abstract. This paper presents a CFD decomposition model for free surface, viscous, incompressible flows related to marine hydrodynamics. The solution decomposition is based on Spectral Wave Explicit Navier Stokes Equations (SWENSE), where the primitive variables are written as the combination of incident and diffracted fields. This allows efficient coupling of the discretised Navier–Stokes free surface flow equations with arbitrary potential flow theories. The domain decomposition is achieved with implicit relaxation zones in order to prevent undesirable wave reflection in unbounded domains. Interface capturing is obtained with implicitly redistanced Level Set (LS) method derived from Phase Field equation. This approach removes the need to redistance the LS field using conventional redistancing procedures and reduces mass conservation issues fundamental to the LS method. The numerical model is based on a polyhedral, second-order accurate, collocated finite volume method (FVM). The coupling of primitive variables is obtained via segregated solution algorithm based on SIMPLE and PISO. The model is implemented in OpenFOAM. The verification of the model is performed by a number of two–dimensional (2–D) test cases. The reflection analysis is carried out by changing the relaxation zone length. Mass conservation and preservation of the signed distance LS function is demonstrated with a simulation lasting 50 incident wave periods. A long domain simulation is also carried out to show that the damping of the wave does not occur. Finally, a wave steepness study has been carried out by changing wave height while the wave period was kept fixed. Three–dimensional (3–D) test cases regarding higher order forces on circular cylinder have also been carried out. However, the results will be presented in future work.

1 INTRODUCTION

Recently, Stern et al. [14] presented an overview of the CFD capabilities related to naval hydrodynamics. A large portion of transient naval hydrodynamic flows is due to ocean waves and their interaction with ships and offshore structures. In this paper, a general decomposition method that couples potential flow and Reynolds–averaged Navier–Stokes (RaNS) model for incompressible, two–phase flow is presented.

Such flows are often modelled with continuity and Navier–Stokes equations. Two–phase flow can be modelled with: Volume of Fluid (VOF) [17], Lagrangian tracking and Level Set (LS) methods [13]. VOF is conservative, but bounded. The LS method based on signed distance function is less mature, but is favourably unbounded. The signed distance character is often preserved by redistancing algorithms [16] or by direct calculation of least distance to the interface in a narrow band [3]. In this paper, a novel method is presented, where the LS equation derived from Phase Field (PF) equation [15] is used. This equation has additional terms that implicitly preserve signed distance function during the solution process. The LS method is suitable for a solution decomposition.

This decomposition is based on the SWENSE method [2], where the unknown fields are decomposed into incident and diffracted components. The incident component is readily available from potential flow theories, while the diffracted component is solved using standard CFD techniques. This method has been successfully applied to both calm water, regular and irregular waves [9], [8]. This proved to be an efficient way of modelling incoming waves in the CFD simulation. In this work, wave reflection has been prevented with relaxation zones first introduced by [5]. The method has been further extended to implicit treatment by Jasak et al. [7].

Numerical discretisation is obtained with a second–order accurate, collocated, polyhedral Finite Volume (FV) method implemented in OpenFOAM. [19]

The paper is organised as follows. In the next section, the mathematical model is discussed. SWENSE decomposition is explained, followed by the description of implicit relaxation zone technique. The numerical model is followed by a set of simulations illustrating stability and accuracy of the wave propagation in an unbounded domain. A conclusion and plans for future work are also given.

2 MATHEMATICAL MODEL

This section presents the mathematical model of incompressible two–phase flow. The model is based on volumetric continuity and Navier–Stokes equations. Two–phase flow is modelled with a LS interface capturing method based on signed distance function. The governing equations are of mixture type, all fields are assumed continuous across the interface.

2.1 Governing equations

Density ρ and dynamic viscosity μ of the mixture are defined with respect to volume fraction, α:

$$\rho = \alpha\rho_w + (1-\alpha)\rho_a \,, \tag{1}$$

$$\mu = \alpha\mu_w + (1-\alpha)\mu_a \,, \tag{2}$$

where subscript w represents water, and subscript a represents air. The relation between LS signed distance function ψ, and volume fraction α will be given below.

2.1.1 Continuity and the Navier–Stokes equations

Ubbink [17] has shown that a volumetric continuity equation can be derived from the phase continuity equation if equation (1) is assumed:

$$\nabla\bullet\mathbf{u} = 0 \,, \tag{3}$$

where $\mathbf{u}$ denotes mixture velocity field.

The Navier–Stokes equation of the mixture [18] reads:

$$\frac{\partial(\rho\mathbf{u})}{\partial t} + \nabla\bullet(\rho\mathbf{u}\mathbf{u}) - \nabla\bullet(\mu\nabla\mathbf{u}) = -\nabla p_d - \mathbf{g}\bullet\mathbf{x}\nabla\rho + \nabla\mathbf{u}\bullet\nabla\mu + \sigma\kappa\nabla\alpha \,, \tag{4}$$

where μ denotes dynamic viscosity, p_d denotes dynamic pressure, $\mathbf{g}$ is the gravitational acceleration vector and $\mathbf{x}$ is the position vector. Additional terms on the right hand side of the equation (4) arise from the two–phase mixture model regarding varying dynamic viscosity across the interface and additional force due to surface tension from Continuum Surface Tension Force (CSF) model by Brackbill [1]. σ denotes surface tension and κ denotes mean interface curvature. A detailed derivation of equation (4) is given by Ubbink [17].

2.1.2 Interface capturing

Two–phase flow modelling is most often achieved with interface capturing methods that use a colour function to capture the location of the interface. Colour function methods often diffuse (smear) the interface over a few computational points to ensure numerical stability. Although possible, reconstruction of the sharp interface from the colour function is not a necessity if the smearing of the interface is confined to a small region. Interface capturing methods can be divided into three major groups: Level Set (LS) methods [13], Phase field (PF) methods [15] and Volume of fluid (VOF) methods, [17]. The most common form of three methods is presented in Figure 1. Water (Ω_1) and air (Ω_2) are

separated by the free surface (Γ). In present work, the LS method is chosen due to its unboundedness and smoothness of the signed distance function defined as:

$$\psi(\mathbf{x}) = \begin{cases} d\,, & \text{if } \mathbf{x} \in \Omega_1\,, \\ 0\,, & \text{if } \mathbf{x} \in \Gamma\,, \\ -d\,, & \text{if } \mathbf{x} \in \Omega_2\,, \end{cases} \tag{5}$$

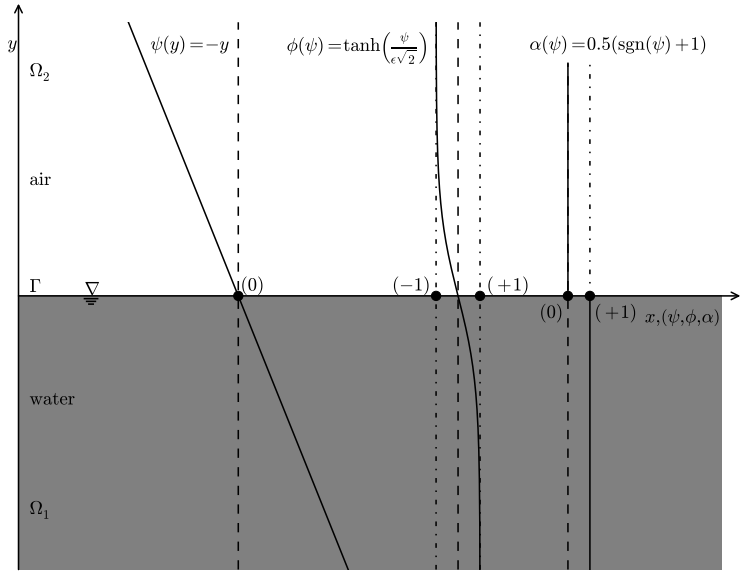

Figure 1: Comparison of interface capturing schemes. ψ is the signed distance function for the Level Set field, ϕ is the Phase Field and α is the volume fraction in the Volume of Fluid approach.

where d is the shortest distance to the interface and $\mathbf{x}$ is the position vector. The interface is located at $\psi(\mathbf{x}) = 0$.

The PF is bounded between -1 and 1 with a prescribed hyperbolic tangent profile across the interface, which in turn depends on the signed distance function:

$$\phi(\psi) = \tanh\left(\frac{\psi}{\epsilon\sqrt{2}}\right), \tag{6}$$

where width parameter ϵ controls the smearing of the interface.

Finally, the VOF method represents a fraction of the volume occupied by water inside

an arbitrary control volume. It defines a sharp interface that can also be defined in terms of LS field:

$$\alpha(\psi) = 0.5\left(\mathrm{sgn}(\psi) + 1\right) , \tag{7}$$

where $\mathrm{sgn}(\psi)$ denotes the signum function. However, the initially sharp interface often gets smeared due to numerical discretisation of convection terms. In order to smoothly calculate fluid properties from equation (1) and (2), a combination of equations (6) and (7) is used:

$$\alpha(\psi) = 0.5\left(\tanh\left(\frac{\psi}{\epsilon\sqrt{2}}\right) + 1\right) . \tag{8}$$

The width parameter ϵ is chosen to smear the interface across two or three cells. This gives sufficient accuracy and numerical stability.

The solution of the usual advection equation for the LS field does not guarantee the preservation of the signed distance function. Hence, redistancing algorithms are often necessary [16]. Redistancing algorithms redistance the LS field after the solution of transport equation, only in the region near the interface. Recently, Sun and Beckermann [15] derived a transport equation for PF that preserves the hyperbolic tangent profile (equation (6)):

$$\frac{\partial\phi}{\partial t} + \mathbf{u}\bullet\nabla\phi = b\left(\nabla\bullet\left(\nabla\phi\right) + \frac{\phi\left(1-\phi^2\right)}{\epsilon^2} - |\nabla\phi|\nabla\bullet\left(\frac{\nabla\phi}{|\nabla\phi|}\right)\right) . \tag{9}$$

The terms on the left hand side (LHS) denote advection. The terms on the right hand side (RHS) of the equation (9) force the PF to preserve hyperbolic tangent profile. Using the relation between PF and LS given by equation (6), equation (9) can be rewritten in terms of LS. The terms on the RHS of equation (9) are then transformed to preserve the signed distance profile of the LS field:

$$\frac{\partial\psi}{\partial t} + \mathbf{u}\bullet\nabla\psi = b\left(\nabla\bullet\left(\nabla\psi\right) + \frac{\sqrt{2}}{\epsilon}\left(1-|\nabla\psi|^2\right)\tanh\left(\frac{\psi}{\epsilon\sqrt{2}}\right) - |\nabla\psi|\nabla\bullet\left(\frac{\nabla\psi}{|\nabla\psi|}\right)\right) . \tag{10}$$

The terms on the LHS are left unaltered. The first term on the right side (RHS) of the equation (10) is a diffusion term that serves to smooth out possible singularities. The second term on the RHS is the curvature–driven motion of the interface. The third term counteracts the second term. Hence, b is a numerical parameter in the absence of curvature driven motion. For detailed discussion on the equation (10), reader is referred to Sun and Beckermann [15].

2.2 SWENSE decomposition

The original SWENSE method introduced by Ferrant [2] decomposes the fields into incident and diffracted components. An arbitrary field (ξ) can be decomposed as:

$$\xi = \xi_I + \xi_D \, , \tag{11}$$

where index I stands for incident field and D is the diffracted field. Note that we take incident and decomposed fields in a general manner. Incident fields are readily available from potential flow theories.

In this approach, velocity and LS fields are decomposed in this manner, while the dynamic pressure is left undecomposed for purposes related to performance. The continuity equation (3) reads:

$$\nabla \bullet \mathbf{u}_D = -\nabla \bullet \mathbf{u}_I \,. \tag{12}$$

The decomposed Navier–Stokes equations (4) read:

$$\begin{aligned} &\frac{\partial(\rho \mathbf{u}_D)}{\partial t} + \nabla \bullet (\rho \mathbf{u}\mathbf{u}_D) - \nabla \bullet (\mu \nabla \mathbf{u}_D) = \\ &- \frac{\partial(\rho \mathbf{u}_I)}{\partial t} - \nabla \bullet (\rho \mathbf{u}\mathbf{u}_I) + \nabla \bullet (\mu \nabla \mathbf{u}_I) - \nabla p_d - \mathbf{g} \bullet \mathbf{x} \nabla \rho + \nabla \mathbf{u} \bullet \nabla \mu + \sigma \kappa \nabla \alpha \,. \end{aligned} \tag{13}$$

The transporting velocity field in the convection term is left unaltered since it is linearised in the solution algorithm. Only the diffracted component is solved for, while the incident components are known at each time step.

The LS equation (10) is first rewritten in the form suitable for FV discretisation.

$$\frac{\partial \psi}{\partial t} + \nabla \bullet (\mathbf{c}\psi) - \psi \nabla \bullet \mathbf{c} - b \nabla \bullet (\nabla \psi) = b \frac{\sqrt{2}}{\epsilon} \tanh\left(\frac{\psi}{\epsilon\sqrt{2}}\right) , \tag{14}$$

where:

$$\mathbf{c} = \mathbf{u} + b \frac{\sqrt{2}}{\epsilon} \tanh\left(\frac{\psi}{\epsilon\sqrt{2}}\right) \nabla \psi + b\kappa \frac{\nabla \psi}{|\nabla \psi|} \,. \tag{15}$$

SWENSE decomposition of the equation (14) gives:

$$\begin{aligned} &\frac{\partial \psi_D}{\partial t} + \nabla \bullet (\mathbf{c}\psi_D) - \psi_D \nabla \bullet \mathbf{c} - b \nabla \bullet (\nabla \psi_D) = \\ &- \frac{\partial \psi_I}{\partial t} - \nabla \bullet (\mathbf{c}\psi_I) + \psi_I \nabla \bullet \mathbf{c} + b \nabla \bullet (\nabla \psi_I) + b \frac{\sqrt{2}}{\epsilon} \tanh\left(\frac{\psi}{\epsilon\sqrt{2}}\right) , \end{aligned} \tag{16}$$

where the last source term is not decomposed since it will not be treated implicitly due to unfavourable effect on the diagonal dominance of the resulting matrix.

The SWENSE decomposition is an efficient model to introduce incoming waves in the CFD simulation. This is done by prescribing $\mathbf{u}_I$ and ψ_I at each time step. Hence, only the diffracted component is solved for.

2.3 Wave reflection suppression

If diffracted components do not vanish near the boundaries, wave reflection will occur. This in turn disrupts the computational results in the domain. Monroy et al. [9] used a coarse computational mesh to damp the diffracted fields and prevent wave reflection. A

general approach based on implicit relaxation zones as implemented by Jasak et al. [7] is used in present work. The relaxation zone volumetrically combines governing equations in order to force diffracted fields to vanish in the far field. Hence, only the incident wave field is present near the boundaries, preventing wave reflection [7].

3 NUMERICAL MODEL

A second–order accurate, collocated FV method with support for arbitrary polyhedral unstructured grids [6] is used in present work. The numerical model is implemented in OpenFOAM. In the present work, all terms regarding diffracted fields are discretised implicitly, leading to a linear system of equations. The discretisation details can be found in [6]. The following discretisation schemes are used:

- Linear blend of Crank–Nicholson [17] and implicit Euler for time derivative;
- Second–order accurate Total Variation Diminishing (TVD) scheme with Van Leer's flux limiter and deferred correction for convective terms;
- Linear interpolation for diffusion terms.

These schemes provide second–order accuracy in space and a blend of first and second–order accuracy in time. The segregated solution algorithm used in present work is a combination of SIMPLE [10] and PISO [4] algorithms. Pressure–velocity coupling is obtained within PISO loop, while the pressure–velocity–LS coupling is obtained in an outer SIMPLE loop. This iterative process is repeated until convergence within each time step.

4 NUMERICAL WAVE TANK

In order to assess the feasibility and drawbacks of presented model, regular wave propagation in numerical wave tank is studied. First, simulation parameters and geometry are presented for a benchmark test case. Next, a reflection study has been carried out by changing relaxation zone length. A long simulation has been carried out in order to assess the conservative properties of implicit relaxation zones and the LS method. A simulation with longer domain has been done to quantify wave damping due to numerical diffusion. Finally, a wave steepness study has been carried out. All results are compared with stream function wave theory [12].

4.1 Benchmark test case

A deep water wave with mild steepness, $ka \approx 0.023$ is simulated. Wave and simulation parameters are given in Table 1.

The block–structured mesh spans from $[0, 60]$ in x direction and $[-6, 0.3]$ in y direction. The mesh consists of three longitudinal and vertical blocks. The cells are strongly graded towards the middle block which is 15 meters ($\approx \lambda$) long and 0.2 meters ($\approx 2H$) high, see

Table 1: Wave and simulation parameters of the benchmark case.

Wave height	H, m	0.1
Wave period	T, s	3
Wave frequency	ω, rad/s	2.0944
Wave length	λ, m	13.934
Wave number	k, m	0.450924
Depth	d, m	6
Relaxation zone length	λ_r, m	22.5
Maximum Courant-Friedrichs-Lewy number	CFL_{max}	0.125
Smearing distance	ϵ	0.004

Figure 2. In the middle block, approximately 15 cells per wave height and 100 cells per wave length are used. The resulting mesh has 11 700 cells.

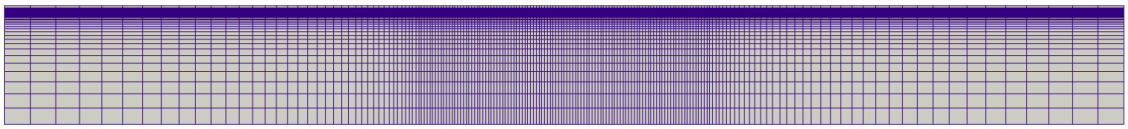

Figure 2: Block–structured, strongly graded mesh.

The relaxation zones are near the inlet and outlet (far field) boundaries. The length of relaxation zones is 22.5 m, or $\lambda_r \approx 1.5\lambda$. Hence, a full CFD solution is obtained in the middle of the domain spanned by 15 meters in the longitudinal direction.

Wave gauges are positioned in the middle part where the full CFD solution is achieved. The longitudinal coordinates are 25, 30 and 35 m for wave gauge 1, 2 and 3, respectively. The simulation time is 30 s (10 periods). Wave elevation signals are processed in the frequency domain. The simulation is initialised with the potential flow solution. Hence, only last five periods are used for Fast Fourier Transform (FFT) in order to neglect any possible transient behaviour at the beginning.

Table 2 to Table 4 present first two harmonics in Fourier series for both CFD solution and stream function wave theory. Only two harmonics are presented while others can be neglected due to the linear nature of this wave. Absolute value of the harmonic is denoted with H_i, where index i stands for order. Real and imaginary parts of the signal are also presented in order to discuss the phase shift. The relative error between solutions is shown in percentages for clarity. Furthermore, normalised relative error is calculated as follows:

$$E_{nr} = E_r \frac{\mathcal{O}(H_2)}{\mathcal{O}(H_1)}\,, \tag{17}$$

Table 2: Fourier representation of wave elevation signals at wave gauge 1.

i^{th} harmonic	CFD solution	Stream function	Relative error, %	Normalised rel. error, %
H_1	$4.9744 \cdot 10^{-2}$	$4.9962 \cdot 10^{-2}$	0.44	0.44
H_2	$5.9138 \cdot 10^{-4}$	$5.8369 \cdot 10^{-4}$	1.32	0.01
$\Re(H_1)$	$1.4242 \cdot 10^{-2}$	$1.3685 \cdot 10^{-2}$	4.07	4.07
$\Im(H_1)$	$4.7662 \cdot 10^{-2}$	$4.8052 \cdot 10^{-2}$	0.81	0.81
$\Re(H_2)$	$-5.0331 \cdot 10^{-4}$	$-4.9623 \cdot 10^{-4}$	1.42	0.01
$\Im(H_2)$	$3.1049 \cdot 10^{-4}$	$3.0734 \cdot 10^{-4}$	1.02	0.01

Table 3: Fourier representation of wave elevation signals at wave gauge 2.

i^{th} harmonic	CFD solution	Stream function	Relative error, %	Normalised rel. error, %
H_1	$4.9695 \cdot 10^{-2}$	$4.9950 \cdot 10^{-2}$	0.51	0.51
H_2	$5.6712 \cdot 10^{-4}$	$5.8299 \cdot 10^{-4}$	2.72	0.03
$\Re(H_1)$	$2.7818 \cdot 10^{-2}$	$2.8595 \cdot 10^{-2}$	2.72	2.72
$\Im(H_1)$	$-4.1179 \cdot 10^{-2}$	$-4.0955 \cdot 10^{-2}$	0.55	0.55
$\Re(H_2)$	$-2.0164 \cdot 10^{-4}$	$-2.0098 \cdot 10^{-4}$	0.33	0.00
$\Im(H_2)$	$-5.3007 \cdot 10^{-4}$	$-5.4726 \cdot 10^{-4}$	3.14	0.03

where $\mathcal{O}(H_1)$ is the order of magnitude of the first harmonic and $\mathcal{O}(H_2)$ is the order of magnitude of the second harmonic. This gives an estimate of relative error's influence on the total solution.

The first harmonic makes up to 99% of the solution. Hence, the second harmonic is smaller by two orders of magnitude. The first row of Table 2 to Table 4 shows that the relative error of the first harmonic is less than approximately 0.5%. The relative error for second harmonic is less than 3%. The phase shift problem is addressed by comparing real and imaginary parts of harmonics. The normalised relative errors for real and imaginary parts of the first harmonic are within 4% for all wave gauges. Generally, errors for real and imaginary parts are greater than errors for the absolute value of certain harmonic. This is expected behaviour when one uses second–order accurate convection schemes [3]. Relative errors of real and imaginary parts of the second harmonic follow the same trend.

Table 4: Fourier representation of wave elevation signals at wave gauge 3.

i^{th} harmonic	CFD solution	Stream function	Relative error, %	Normalised rel. error, %
H_1	$4.9881 \cdot 10^{-2}$	$4.9963 \cdot 10^{-2}$	0.16	0.16
H_2	$5.7767 \cdot 10^{-4}$	$5.8388 \cdot 10^{-4}$	1.06	0.01
$\Re(H_1)$	$-4.9657 \cdot 10^{-2}$	$-4.9825 \cdot 10^{-2}$	0.34	0.34
$\Im(H_1)$	$4.7145 \cdot 10^{-3}$	$3.7095 \cdot 10^{-3}$	27.09	2.71
$\Re(H_2)$	$5.6879 \cdot 10^{-4}$	$5.7743 \cdot 10^{-4}$	1.50	0.02
$\Im(H_2)$	$-1.0090 \cdot 10^{-4}$	$-0.8653 \cdot 10^{-4}$	16.61	0.17

4.2 Reflection study

The reflection study has been carried out in order to determine the length of relaxation zones needed to prevent wave reflection. The relaxation zones are positioned at the inlet and outlet boundaries. In the relaxation zones, the diffracted components are damped to zero, leaving a full potential flow solution. The relaxation zone length, λ_r was varied from 0.5λ to 1.5λ. The evolution of wave elevation for different wave gauges shows similar behaviour. Hence, only wave gauge 2 is analysed in the frequency domain.

The first harmonics are presented in Table 5. If other uncertainties and numerical errors are neglected, the relative error of first order harmonics is an estimate for the amplitude of the reflected wave. The phase speed of the wave is approximately 4.64 m/s, making the simulation time of 30 s enough for reflected wave to travel through the domain more than two times. The relative error of the magnitude of first order harmonics converges to zero by increasing relaxation zone length. The relative error for the first order harmonic rapidly decreases from approximately 5% with $\lambda_r = 0.5\lambda$ to less than 2% with $\lambda_r = 0.75\lambda$. Relaxation zone lengths greater than λ give an estimate for the reflected wave below 1%. At this point, it cannot be clear if the reflection occurs, because the numerical error presented in previous study persist. Apart from the magnitude, the relative errors for real and imaginary parts are calculated in order to address the phase shift related to wave reflection. As can be seen from Table 5, the phase shift problem decreases with increasing relaxation zone length, since the real and imaginary parts of the first order harmonic show monotone convergence.

4.3 Long simulation stability assessment

Stability, mass conservation and accuracy of the presented algorithm is assessed with a very long solution of the benchmark case defined in Table 1. The simulation time was 150 seconds, which corresponds to 50 wave periods. For all wave gauges, the Fourier analysis over last 45 periods gave results that are almost identical to ones presented in Table 2

Table 5: First harmonic for different relaxation zone lengths, λ_r at wave gauge 2.

λ_r	$H_1 \cdot 10^2$	$\Re(H_1) \cdot 10^2$	$\Im(H_1) \cdot 10^2$	$E_r(H_1)$	$E_r(\Re)$	$E_r(\Im)$
0.5λ	4.7512	2.2031	-4.2096	4.88	22.96	2.78
0.75λ	4.9023	2.2565	-4.3521	1.86	21.09	6.27
1λ	4.9493	2.6044	-4.2087	1.21	8.92	2.76
1.25λ	4.9344	2.6598	-4.1562	0.91	6.98	1.48
1.5λ	4.9635	2.7582	-4.1266	0.63	3.54	0.76
Stream function	4.9950	2.8595	-4.0955	0.00	0.00	0.00

to Table 4. The difference was in the fourth significant digit for both real and imaginary parts of first harmonics, that is $\approx 0.1\%$. Mean water level rise is approximately 0.00001%, which is considered negligible.

In the LS method, the preservation of the signed distance function is of crucial importance for both mass conservation and correct interface reconstruction. This is demonstrated in Figure 3 which presents the LS field in the middle part of the domain bounded by $x \in [29, 30]$ and $y \in [-0.4, 0.4]$ m. The interface is denoted with white line. Ten black lines denote iso–contours of the LS field equally spaced between -0.2 and 0.2. The signed distance character of the LS field is very well preserved, both near the interface and far away.

The duration of the simulation was 3 hours and 25 minutes on an Intel Core i7-4820K CPU at 3.70GHz for 50 wave periods, or approximately 4 minutes per period.

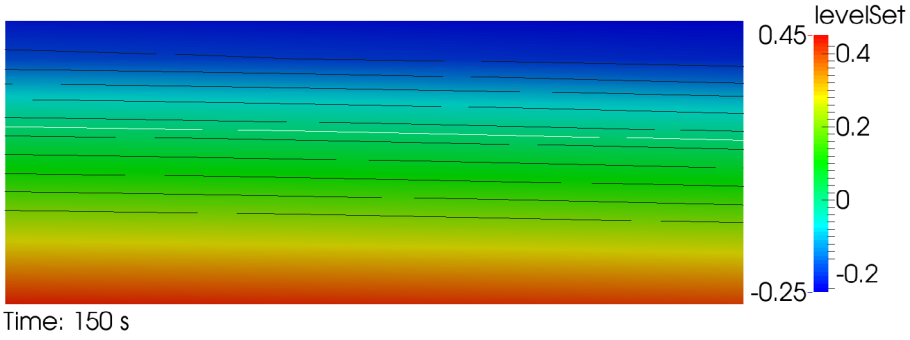

Figure 3: Preservation of the signed distance function: last period, $t = 150$ s.

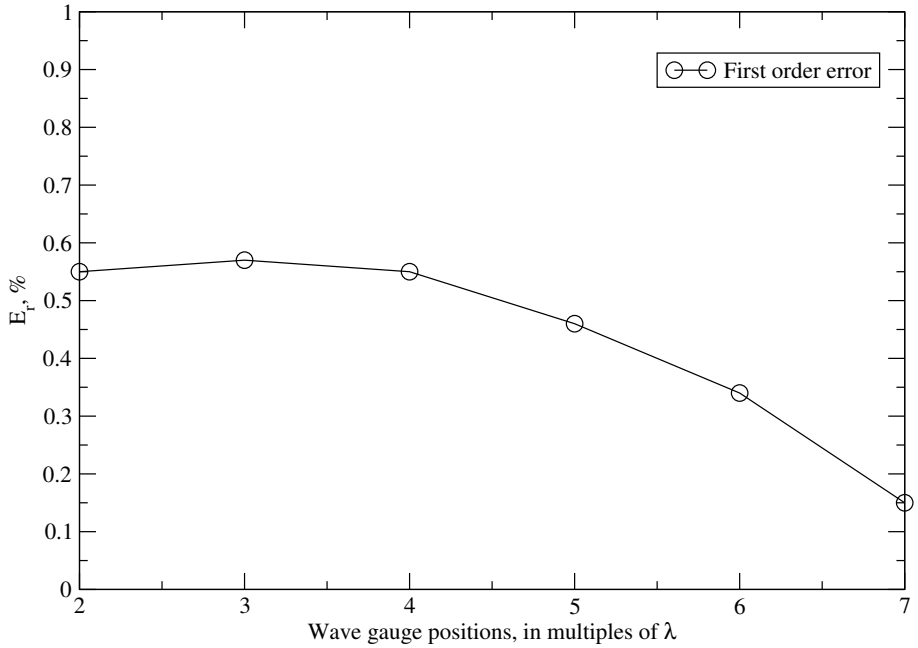

Figure 4: Relative errors for first harmonic compared to stream function wave theory, given for wave gauges at different multiples of λ.

4.4 Long domain simulation

A long domain simulation has been carried out in order to assess numerical diffusion related to wave propagation. The wave parameters are the same as in the original benchmark case presented in Table 1. The only difference is the domain which now spans from 0 to 120 m in the longitudinal direction. The relaxation zone length is left unaltered at 22.5 m. The middle part of the domain where 100% of CFD solution is present contains approximately 5.5 wave lengths. In this region, 100 cells per wave length and 15 cells per wave height are used which is the same as in the mesh used in the benchmark case (Figure 2). 6 wave gauges are used to measure wave elevation at different multiples of λ: from 2λ to 7λ. The relative error for first order harmonic is presented in Figure 4 for different wave gauge positions given in multiples of λ. The figure shows that the relative error decreases further away from the inlet. This decrease is quite small ($\approx 0.3\%$) while the relative error stays within $\approx 0.6\%$, demonstrating insensitivity to simulation with longer domain.

4.5 Wave steepness study

Wave steepness can be represented by dimensionless number, ka where k is the wave number in rad/s and a is the amplitude of the wave in m. The non–linearity of wave increases with increasing steepness. In this work, wave height is gradually increased while

the wave period, T is fixed to 3 s. The wave height is varied from 0.2 to 1.6 m, giving a steepness range from 0.045 to 0.325 according to stream function wave theory. For each case, the total cell count in the mesh remained constant (11 700). However, blocks were changed such that there are always 15 cells per wave height and 100 cells per wave length in the middle of the domain. This way, the mesh is similar to the one used in previous studies.

Table 6: Wave parameters for steepness study.

Index	Wave amplitude	Wave length	Wave number	Steepness
i	a, m	λ, m	k, rad/s	ka
1	0.1	13.9546	0.4503	0.04503
2	0.2	14.0360	0.4477	0.08953
3	0.3	14.1688	0.4435	0.13304
4	0.4	14.3488	0.4379	0.17516
5	0.5	14.5714	0.4312	0.21560
6	0.6	14.8314	0.4236	0.25418
7	0.7	15.1236	0.4155	0.29082
8	0.8	15.4427	0.4069	0.32550

Both the stream function wave theory and the present model capture higher order effects with increasing steepness. Relative errors of first and second order harmonics are presented in Figure 5. The relative error for first order harmonics gradually increases with steepness. However, the relative error is always below 7%. The relative error for second order harmonics oscillates within narrow band (less than 3%) for waves up to $ka = 0.25$. For very steep waves, the error is about 4%. Third order errors show the similar trend to first order ones.

Wave steepness is varied by changing the wave height. This leads to very large velocities below the crest of the wave for steepest waves. These velocities in turn cause parasitic air velocities because the interface jump conditions as explained in [3] or [11] are not yet implemented. Nevertheless, the implementation of interface jump conditions will be the topic for future work. Authors believe that this could explain larger relative errors for very steep waves.

5 CONCLUSION

A decomposition model for wave–like flows for naval hydrodynamics is described. The interface capturing is achieved with the implicitly redistanced Level Set method. The solution is decomposed using a variant of the SWENSE method, where the field is regarded as the sum of incident and diffracted fields. The incident wave field is obtained

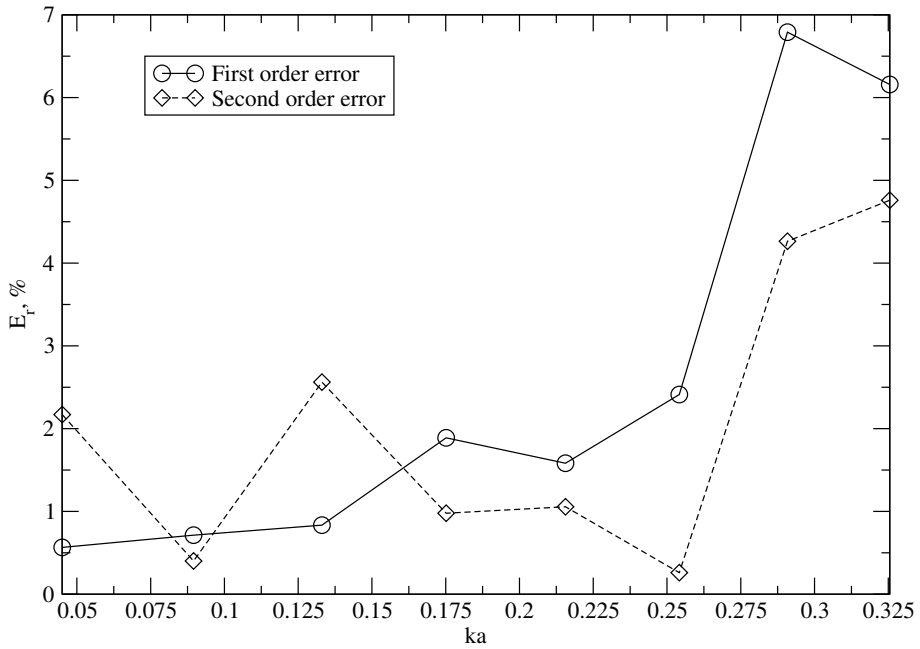

Figure 5: Relative errors for first and second order harmonics compared to stream function wave theory.

with low–cost potential flow wave theory, while the diffracted component is solved. The domain is decomposed using implicit relaxation zones that damp the diffracted fields to zero near the boundaries. This prevents wave reflection. The solution algorithm is based on second–order accurate, polyhedral FV method with segregated approach, implemented in OpenFOAM.

As a preliminary study, 2–D wave propagation is assessed and compared to stream function wave theory in the frequency domain. The magnitudes of the first harmonics were within 1%, and within 3% for real and imaginary parts. This indicates a minor phase shift difference as often encountered in CFD. The reflection study has been carried out with varying relaxation zone length. The relaxation zone that is one wave length long gave reflection estimate of 1%. A very long simulation that lasted 50 wave periods demonstrated good conservative properties of the LS method and implicit relaxation zones, as well as the preservation of the signed distance function. The dissipation of the propagating wave did not occur in an 8 wave lengths long domain. The wave steepness study demonstrated good results for wide range of steepness parameters. However, it indicated problems for very steep waves ($ka > 0.25$) that could be related to parasitic air velocities. These velocities could be resolved by consistent implementation of interface jump conditions, which will be considered in future study.

Results of higher order forces on circular cylinder will be presented in future work.

REFERENCES

[1] J.U. Brackbill, D.B. Kothe, and C. Zemach. A continuum method for modelling surface tension. *J. Comput. Phys.*, 100:335–354, 1992.

[2] P. Ferrant. *Modélisation en Hydrodynamique à Surface Libre*. PhD thesis, Ecole Centrale de Nantes, 2006.

[3] J. Huang, P. M. Carrica, and F. Stern. Coupled ghost fluid/two–phase level set method for curvilinear body–fitted grids. *Int. J. Numer. Meth. Fluids*, 44:867–897, 2007.

[4] R. I. Issa. Solution of the implicitly discretised fluid flow equations by operator-splitting. *Journal of Computational Physics*, 62:40–65, 1986.

[5] N. G. Jacobsen, D. R. Fuhrman, and J. Fredsøe. A wave generation toolbox for the open-source CFD library: OpenFoam®. *Int. J. Numer. Meth. Fluids*, 70(9):1073–1088, 2012.

[6] H. Jasak. *Error Analysis and Estimation for the Finite Volume Method with Applications to Fluid Flows*. PhD thesis, Imperial College of Science, Technology & Medicine, London, 1996.

[7] H. Jasak, V. Vukčević, and I. Gatin. Numerical Simulation of Wave Loads on Static Offshore Structures. In *CFD for Wind and Tidal Offshore Turbines - in press*, pages ??–?? Springer Tracts in Mechanical Engineering, 2015.

[8] R. Marcer, C. Audiffren, C. Dassibat, de Jouette C., and P. E. Guillerm. Sea-keeping modelling in calm water and in waves using the CFD code Eole. In *11ème Journées de l'Hydrodynamique*, pages 1–12, April 2007.

[9] C. Monroy, G. Ducrozet, A. Bonnefoy, A. Babarit, and P. Ferrant. RANS simulations of a CALM buoy in regular and irregular seas using the SWENSE method. In *Proceedings of the Twentieth International Off–shore and Polar Engineering Conference*, pages 678–685, June 2010.

[10] S. V. Patankar and D. B. Spalding. A calculation procedure for heat, mass and momentum transfer in three-dimensional parabolic flows. *International Journal of Heat and Mass Transfer*, 15:1787–1806, 1972.

[11] P. Queutey and M. Visonneau. An interface capturing method for free–surface hydrodynamic flows. *Computers & Fluids*, 36:1481–1510, 2007.

[12] M. M. Rienecker and J. D. Fenton. A Fourier approximation method for steady water waves. *J. Fluid. Mech.*, 104:119–137, 1981.

[13] J. A. Sethian. *Level Set Methods: Evolving Interfaces in Geometry, Fluid Mechanics, Computer Vision and Materials Science*. Cambridge University Press, 1996.

[14] F. Stern, J. Yang, Z. Wang, H. Sadat-Hosseini, M. Mousaviraad, Bhushan S., and T. Xing. Computational Ship Hydrodynamics: Nowadays and Way Forward. In *Proceedings of the 29th Symposium on Naval Hydrodynamics*, pages 1–73, August 2012.

[15] Y. Sun and C. Beckermann. Sharp interface tracking using the phase–field equation. *Journal of Computational Physics*, 220:626–653, 2007.

[16] M. Sussman and E. Fatemi. An efficient, interface-preserving level set redistancing algorithm and its application to interfacial incompressible fluid flow. *Journal of Scientific Computing*, 20(4):1165–1191, 1999.

[17] O. Ubbink. *Numerical prediction of two fluid systems with sharp interfaces*. PhD thesis, Imperial College of Science, Technology & Medicine, London, 1997.

[18] V. Vukčević, A. Östman, and H. Jasak. Rapid Simulations of Pure Sway Motion Using FVM in OpenFOAM. In *SIMMAN 2014: Workshop on Verification and Validation of Ship Manoeuvring Simulation Methods*, December 2014.

[19] H. G. Weller, Tabor. G., and H. Jasak. A tensorial approach to computational continuum mechanics using object oriented techniques. *Computers in Physics*, 12:620–631, 1998.